Black Phosphorus Carbide as a Tunable Anisotropic Plasmonic Metasurface

Xin Huang,[†,‡] Yongqing Cai,[§] Xuewei Feng,[†,‡] Wee Chong Tan,[†,‡] Dihan Md. Nuruddin Hasan,[†] Li Chen,[†,‡] Nan Chen,[†] Lin Wang,[†,‡] Li Huang,[†,‡] Thorin Jake Duffin,[‡,∥,⊥] Christian A. Nijhuis,[‡,∥,⊥,#] Yong-Wei Zhang,[§] Chengkuo Lee,[†] and Kah-Wee Ang*[†,‡]

†Department of Electrical and Computer Engineering, National University of Singapore, 4 Engineering Drive 3, 117583, Singapore

‡Centre for Advanced 2D Materials, National University of Singapore, 6 Science Drive 2, Singapore 117543, Singapore

§Institute of Higher Performance Computing, 1 Fusionopolis Way, 138632 Singapore

∥Department of Chemistry, National University of Singapore, 3 Science Drive 3, Singapore 117543, Singapore

⊥NUS Graduate School for Integrative Sciences and Engineering, National University of Singapore, 28 Medical Drive, Singapore 117456, Singapore

#NUSNNI-Nanocore, National University of Singapore, Singapore 117411, Singapore

Ⓢ *Supporting Information*
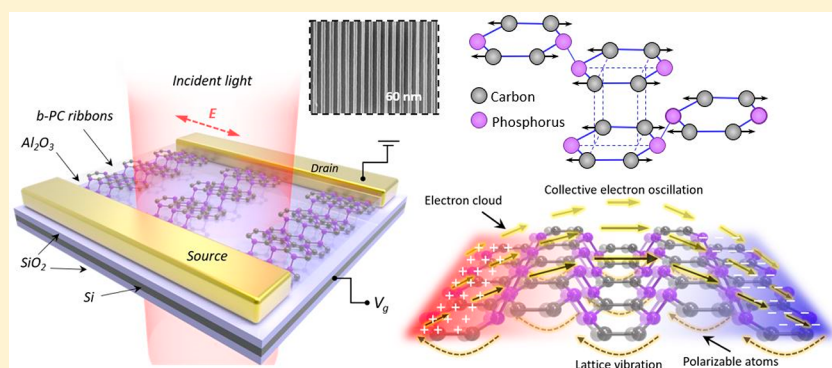
ABSTRACT: Tailoring photonics for monolithic integration beyond the diffraction limit opens a new era of nanoscale electronic-photonic systems, including graphene plasmonics which exhibits low level of losses and high degree of spatial confinement. Limited to its isotropic optical conductivity, searching for new plasmonic building blocks which offer tunability and design flexibility beyond graphene is becoming quite crucial for next-generation optoelectronic device. Here, motivated by the recent emergence of a new 2D material, we develop a mid-infrared (mid-IR) metasurface by nanostructuring a thin layer of black phosphorus carbide (b-PC) and realize efficient excitation of hybrid plasmon mode at deep subwavelength-scale. Far-field infrared spectroscopy demonstrates that the hybrid plasmon mode displays an anticrossing behavior of two splitting optical modes, which can be attributed to the Fano resonance between plasmons and IR-active optical phonons in b-PC. Significantly, it further presents a strong anisotropic behavior along different crystal orientations, which arises from its peculiar puckered lattice structure with two clearly distinguishable axes. The results illustrate that anisotropic b-PC plasmon not only represents an important advance in subwavelength optoelectronics, but also provides a viable platform for hyperbolic metamaterials, bringing widespread applications into biosensors, single-photon source, nanoantenna, and subwavelength resolution imaging.

KEYWORDS: *hybrid plasmon mode, anisotropic dispersion, black phosphorus carbide, nanoribbon arrays, Fano resonance*

Nanoscale light−matter interaction through a plethora of dipole-type excitations has been widely studied in two-dimensional (2D) layered materials.[1] In graphene, highly confined and electrically tunable hybrid modes, that is, surface plasmon-polaritons (SPPs) or hybrid plasmon-phonon-polaritons (HPPPs), have stimulated considerable research efforts, including tunable terahertz metamaterials,[2] plasmonic waveguides,[3] ultrasensitive photodetector,[4] and mid-infrared biosensing.[5,6] Motivated by these advancements, great efforts have

been devoted to discovering and exploring new plasmonic effects beyond graphene, particularly, black phosphorus (b-P). Several theoretical works have already demonstrated that the optical conductivity and collective electronic excitations may exhibit a strong anisotropy in such a system.[7−9] However, to the best of our knowledge, except for the near-field optical
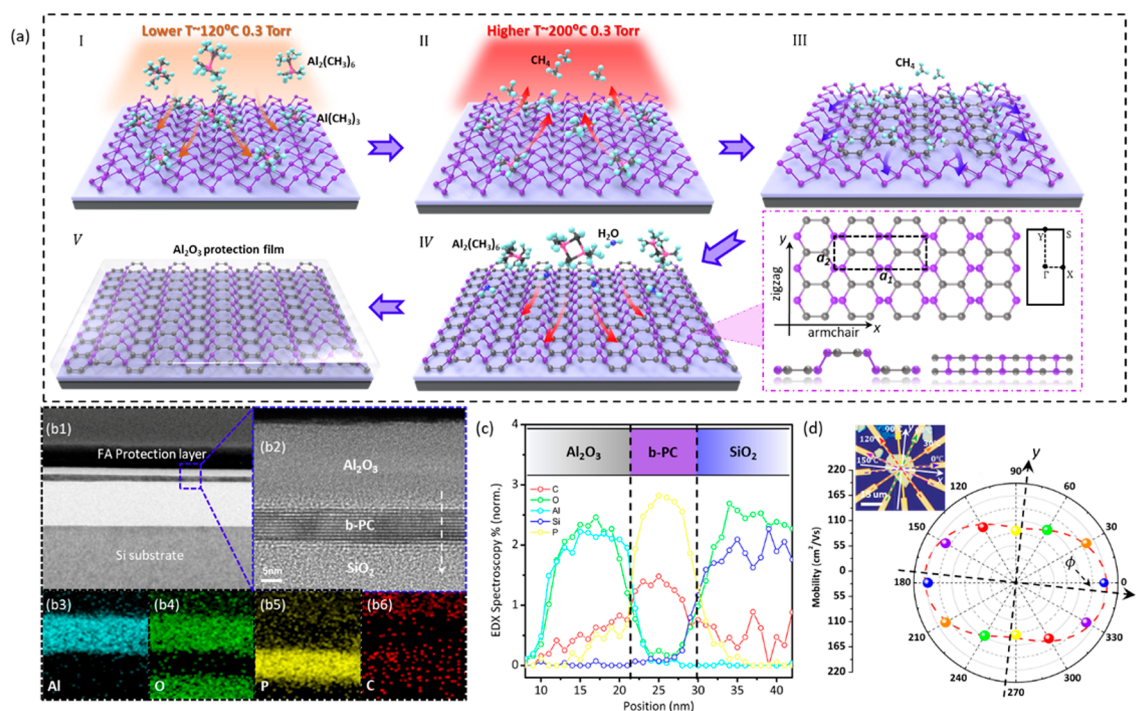
Figure 1. Synthesis and material characterization of b-PC. (a) Schematic diagram describing the synthesis of b-PC via carbon doping on b-P. Inset: the structural geometry of α-phase of b-PC, including top view, side view (along armchair and zigzag direction), and the Brillouin zone. The lattice unit is marked by the black dotted line, a_1 (8.68 Å) and a_2 (2.92 Å) are the lattice constants along x- and y-direction, respectively. (b1) HAADF-STEM image of Al_2O_3/b-PC/SiO_2. (b2) The magnified HR-TEM image collected from the labeled area in (b1). (b3−b6) EDX elemental mapping of the Al_2O_3/b-PC/SiO_2 cross-section, and (c) corresponding EDX line profiles (along the direction of dotted arrow in b2) for Al (cyan), O (green), P (yellow), and C (red) elements. (d) Angle-resolved DC mobility along the six directions and circles of the same color corresponds to the directions indicated by the arrows in the inset. Inset: an optical micrograph of b-PC flake with a thickness of around 20 nm. A total of 12 electrodes (5 nm Ti/60 nm Au) were fabricated on the same flake spaced at an angle of 30°.

imaging of plasmons in b-P[10] and SiO_2/b-P/SiO_2 heterostructure,[11] the fundamental behavior of anisotropic plasmon resonance is rarely studied in experiment, and the design of plasmonic metamaterials using patterned b-P nanostructures has not been explored. Determined by its plasmonic Drude weight,[7] the challenge still remains for far-field optical imaging of intrinsic b-P plasmons because of its larger effective mass of electrons/holes and insufficient carrier densities compared to the semimetallic graphene.

As one of the emerging classes of 2D materials, black phosphorus carbide (b-PC), a compound analogue of graphene and phosphorene, has a buckled honeycomb lattice. Its highly anisotropic band structure and finite bandgap make it a potential candidate for future generations of electronics/optoelectronics.[12] Recently, Tan et al. reported a high-performance composite few-layer b-PC field-effect transistor fabricated via a novel carbon doping technique. A high hole mobility is achieved at room temperature due to the small effective mass of the electrons/holes in b-PC, which is predicted to have one of the lightest electrons/holes among all known 2D materials.[13] According to the structural similarities that exist between graphene and b-P, the following intriguing questions arise: is it possible for b-PC to serve as a promising plasmonic material for manipulating electromagnetic (EM) signals at the deep-subwavelength scale? If yes, is there any opportunity to incorporate the anisotropic band dispersion of b-PC into the lattice-orientation-dependence for intrinsic plasmons?

In this work, we perform the far-field optical characterization of few-layer b-PC nanoribbon arrays at mid-infrared (mid-IR)

spectrum, revealing a new HPPP mode which arises from both phonon-like and plasmon-like characteristics. HPPP excitation is evidently identified by IR transmission spectroscopy, with the resonant frequency tuned in situ, through electrostatic doping or nanoribbon width. The new HPPP mode is explained by the coupling between collective electron oscillations and the IR-active optical phonon vibrations in few-layer b-PC with AB stacking configuration. More remarkably, in contrast to the isotropic plasmon−phonon interactions in graphene-based van der Waals heterostructures,[14,15] the HPPP mode in b-PC nanoribbon strongly disperses along different lattice orientations due to its in-plane electronic mass anisotropy, demonstrating a prominent redshift of plasmon frequency from armchair to zigzag direction. Furthermore, the experimental results show excellent agreement with numerical calculations using random phase approximation (RPA) theory and finite element method (FEM). The proposed implementation based on b-PC nanoribbons exploits the intrinsic in-plane anisotropy of this material to realize the functionality of its plasmons and demonstrate important advantage over isotropic 2D materials like graphene, eventually hinting at enormous potential for future applications such as ultrafast plasmonic circuits,[16] planar hyperlens,[17] and optical communication systems.[18]

The synthesis of the b-PC via carbon doping technique is briefly described in Figure 1. The b-P flake (purity 99.998%, Smart Element) is mechanically exfoliated onto a lightly doped SiO_2 (90 nm)/Si substrate and immediately transferred into the atomic layer deposition (Savannah ALD) chamber. First, trimethylaluminum (TMA), that is, $Al_2(CH_3)_6$ precursor is
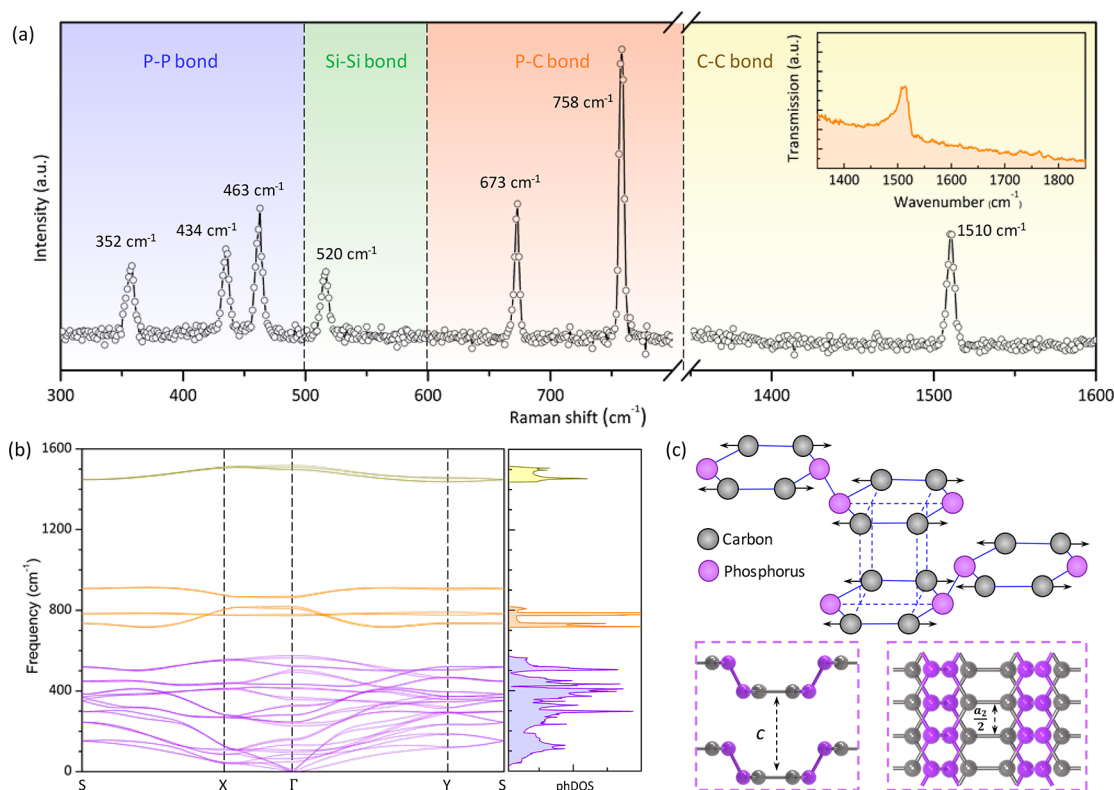
Figure 2. Micro-Raman spectroscopic characterization of few-layer b-PC flake. (a) Raman spectra of b-PC, showing four major regimes labeled by different colors, including P−P bond (purple), Si−Si bond (green), P−C bond (orange), and C−C bond regimes (yellow). Inset: a mid-IR transmission spectrum of b-PC on SiO_2 normalized relative to transmission through the SiO_2/Si substrate. (b) The phonon dispersion and phonon density of states calculated for bulk b-PC using DFPT along the high symmetry directions in the first Brillouin zone. (c) Illustration of atomic displacements for Γ−point phonon mode of 1510 cm^{-1} in b-PC with AB stacking configuration. Purple and gray circles represent the P and C atoms, respectively. Black lines denote the relative position of carbon atoms from neighboring two layers. The dotted line box shows the side view and top view of AB-stacked b-PC are marked by the dotted line and c (10.763 Å) denotes the distance between two neighboring layers.

repeatedly pulsed and purged under a chamber temperature of 120 °C and a pressure of 0.3 Torr, leading to the dissociation of TMA dimers into monomers ($Al(CH_3)_3$; Step I). Then, the chamber temperature is increased to 200 °C and subsequently caused one of the methyl groups in the $Al(CH_3)_3$ to react with a hydrogen on another methyl group, liberating methane, CH_4 as a free radical (Step II). With the release of CH_4, there is now a free radical CH_4 available to break the phosphorus− phosphorus (P−P) bonds in b-P and allow the carbon atom in CH_4 to form the phosphorus−carbon (P−C) bonds (Step III). Finally, the TMA is repeatedly purged again with H_2O together to form an overlying Al_2O_3 passivation layer (Steps IV and V). According to previous works, it implies that different phases of P_xC_{1-x} monolayer are possible to be synthesized in experiment.[12] Among them, the stoichiometric monolayers (x = 0.5) are predicted to be more stable configurations, including α-, β-, and γ-phases.[12] Inspired from previous works,[13,19] the semiconducting α-phase, which is the lowest-energy phase of b-PC, is represented in this work. As shown in Figure 1, the α-phase of b-PC monolayer has a puckered surface in hexagonal networks, consisting of C and P atoms bonding with three nearest neighbors though sp^2 and sp^3 hybridization, respectively. The cross-section high-angle annular dark-field scanning transmission electron microscopy (HAADF-STEM) image of synthesized b-PC flake is presented in Figure 1b1. Figure 1b2 shows the high-resolution transmission electron microscopy (HR-TEM) image collected from the labeled area (Figure 1b1) and it characterizes the vertical alignment of different layers,

clearly demonstrating the boundaries of crystalline few-layer b-PC sandwiched by the top Al_2O_3 passivation layer and bottom SiO_2 substrate. STEM energy-dispersive X-ray spectroscopy (EDX) elemental mapping (Figure 1b3−b6) reveals the spatial distributions of Al, O, P, and C elements, confirming that the contrasts in Figure 1b2 are a result from the variation of chemical compositions. The corresponding line profile extracted from EDX mapping is displayed in Figure 1c and it is found that the peak of C atomic concentration locates around the b-PC and slowly decreases along b-PC thickness toward the b-PC/SiO_2 interface. Similar to b-P, the puckered structure also endows b-PC a highly anisotropic behavior at Γ point of reciprocal lattice (inset in Figure 1a), with in-plane armchair along the x-direction and zigzag along the y-direction. Angle-resolved DC mobility measurements further validate its in-plane electronic mass anisotropy in b-PC. In this experiment, 12 electrodes (5 nm Ti/60 nm Au) were fabricated on the same flake spaced at an angle of 30° along the directions as shown in the inset of Figure 1d. The 0° reference direction was selected arbitrarily. These DC mobility measurements were performed by applying electrical field across each pair of diagonally positioned electrodes at 180° apart and the results were plotted in polar coordinates in Figure 1d. The directional dependence of mobility in an anisotropic b-PC is fitted by the equation (red dotted curve): $\mu_\theta = \mu_x \cos^2(\theta - \phi) + \mu_y \sin^2(\theta - \phi)$, where μ_x and μ_y refer to the mobility of b-PC along x- and y-directions, respectively. θ is the angle with respective to the 0° reference direction and $\phi = -6°$ gives the best fit for the measurement.
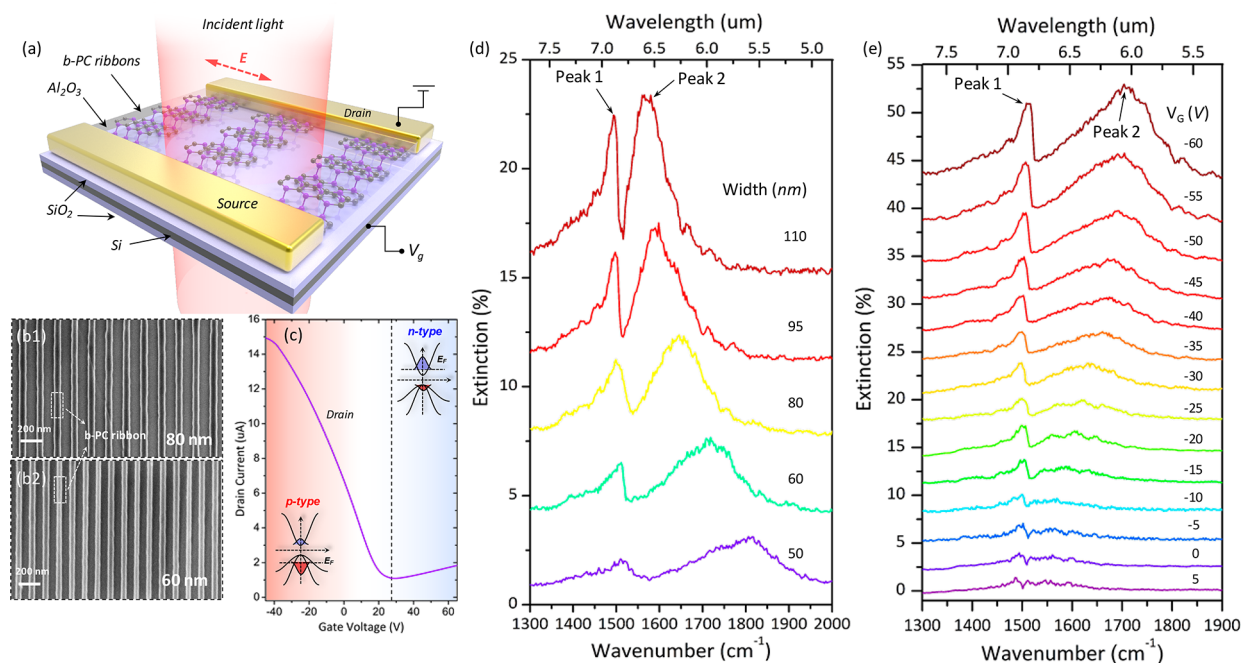
Figure 3. Schematic diagram for mid-IR transmission measurement of back-gated b-PC nanoribbon arrays by FTIR microscopy. (a) The excitation light is broadband and polarized perpendicular to the b-PC nanoribbons. The b-PC sheet is grounded though Ti (5 nm)/Au (60 nm) that serves as source-drain contacts, allowing for in situ measurement of the b-PC electrical current. (b1) and (b2) SEM image of a typical array of 80 and 60 nm b-PC nanoribbons. (c) Room temperature transfer characteristic, I_d−V_g curve of b-PC nanoribbon transistor, showing a bottom in the drain current at the CNP (charge neutral point). (d) Width dependence of optical transmission through b-PC ribbon with V_g = −40 V. The width is varied from 50 to 110 nm. (e) Gate-induced modulation of transmission through 80 nm wide b-PC nanoribbon, with back-gate voltage from +5 V to −60 V. All of transmission spectra were normalized to the one obtained at the CNP.

Figure 2a shows the Raman spectrum of b-PC in back-scattering configuration (Alpha 300R). The wavelength of laser is 532 nm and the spot size is ≈1 μm. According to the lattice structure of b-PC, several different bonds may exist and therefore we divide its Raman spectrum into three major regimes, including P−P, P−C, and C−C bond regimes. Specifically, three peaks including 352, 434, and 463 cm^{-1}, which correspond to homoatomic P−P bond remain similar to the characteristic peaks from b-P, except for a slight redshift. Two prominent phonon modes at 673 and 758 cm^{-1} are indicative of the P−C bond, based on the theoretical calculations (670−780 cm^{-1}) reported in the literature.[20] Another peak of 1510 cm^{-1}, which is close to the G mode of graphite around 1580 cm^{-1}, can be attributed to the bond stretching motion of the pairs of C sp^2 atoms in b-PC, as shown in Figure 2c. Comparing with the G mode of graphite, the b-PC peak shifts to lower wavenumber due to the π-p* conjugation, thus suggesting the formation of P−C bonds.[21] Among the various stacking possibilities of few-layer b-PC, previous works reported that the most stable configuration is AB stacking with a half-lattice shift of $a_2/2$ along a_2 direction (Figure 2c).[13] Figure 2b presents the phonon dispersion for AB-stacked bulk b-PC, calculated by density functional perturbation theory (DFPT) along the high symmetry directions in the first Brillouin zone (see the Section 1 in Supporting Information). Previous work confirms that the maximum vibrational frequency around 1510 cm^{-1} for the optical branch of b-PC is associated with C atoms and is consistent with our calculated phonon density of states (phDOS) affirming a high strength of C−C bonds.[12] Moreover, an IR microscope coupled to a Fourier transform infrared spectrometer (FTIR) was used to measure the transmission spectrum of b-PC on SiO$_2$ and

normalized relative to transmission through the SiO$_2$/Si substrate (in the inset of Figure 2a). Noticeably, the b-PC spectrum is flat except for a narrow peak that occurs at around 1510 cm^{-1}, which has not been reported before. In fact, the AB stacking configuration of b-PC leads to the breaking of inversion symmetry, therefore inducing a net macroscopic dipole moment of C−C sp^2 bond stretching motion.

In order to achieve strong mid-IR plasmon excitation, we fabricated the periodic b-PC nanoribbon arrays (with thickness of ~18 nm), as illustrated in Figure 3a (not to scale). For the investigation of principal plasmon behavior in b-PC, all of nanoribbon widths were fabricated along the armchair direction and the lattice-orientation-dependence for plasmons would be discussed in the following part. Using this process, we were able to fabricate armchair-oriented b-PC with ribbon width ranging from 50 to 110 nm (see the Supporting Information for details). In order to eliminate the ribbon-to-ribbon coupling effect, the b-PC nanoribbons were electronically continuous with a width to gap ratio of 1:1.5,[22] as shown in the scanning electron microscopy (FEI Verios 460 SEM) image in Figure 3b1,b2. Figure 3c displays a typical gate-dependent I−V curve for our device. The bottom in the I−V curve corresponds to the charge neutral point (CNP) of the b-PC, when the Fermi level aligns with middle of bandgap and the carrier density is minimized. The b-PC at zero gate voltage is found to be highly p-type doped and this can be ascribed to both defects[23] and carbon doping effect.[12]

Next, the device was then placed in a FTIR microscope and measured in transmission mode with incident light polarized perpendicular to b-PC nanoribbon. The extinction spectra are given by the normalized transmission spectra T relative to the one at the CNP (T_{CNP}) as $1 − T/T_{CNP}$. Figure 3d presents the
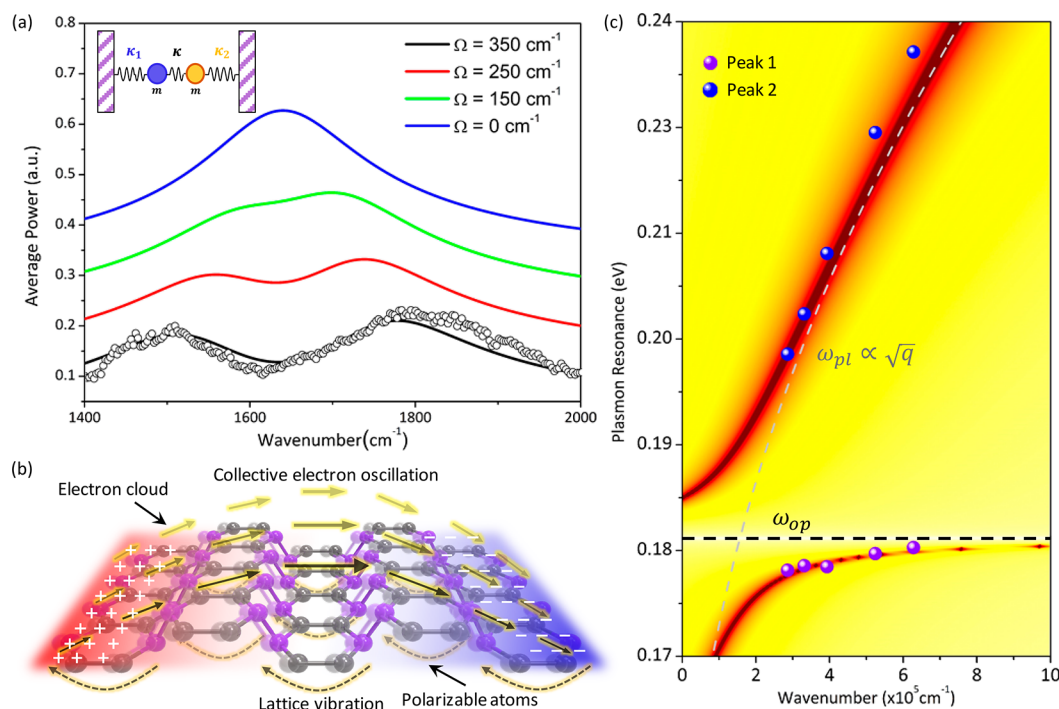
Figure 4. Schematics of mechanism responsible for the plasmon−phonon coupling in b-PC ribbon. (a) Phenomenological model of two coupled classical oscillators with a series of coupling strength and best performance can be obtained using coupling strength of 350 cm^{-1} to fit the extinction spectrum of b-PC nanoribbon array with W = 50 nm. The inset depicts the coupled oscillator mode scheme which is discussed in detail in the Supporting Information. (b) Schematic diagram to explain the physical mechanism behind the plasmon−phonon coupling in b-PC ribbon. (c) Plasmon frequency as a function of wavenumber for peaks 1 and 2. The experimental results are extracted from Figure 3d (purple and blue square dots for peaks 1 and 2, respectively). The calculated dispersion relation is represented by the loss function and is plotted as a 2D pseudocolor background.

extinction spectra of b-PC nanoribbon arrays with ribbon width (W) from 50 to 110 nm, while the gate voltage is biased at −40 V. Two prominent resonance peaks within our measured frequency range of interest (1250−2000 cm^{-1}) are revealed, which includes a sharp resonance around the optical phonon mode 1510 cm^{-1} (ω_{op}) and another broader peak. Analogous to the HPPP in graphene,[24] we can identify three key trends in the spectra. The first is dispersion: both of the peaks blueshift as W decreases, but at very different rates. In particular, peak 2 disperses to higher frequencies at a much faster rate. The second trend is line width: both line widths of peak 1 and peak 2 increase with decreasing W. The line width is directly related to plasmon damping and its damping effect may increase as W decreases, indicative of more carrier scattering at the edges of ribbon.[25] The third trend is an anticrossing behavior of the spectral weight, which reveals a relative shift of peak 1 transferred to peak 2 as W decreases. To better understand the origin of these two features, we further studied the dependence of transmission spectra on carrier density tuned in situ by electrostatic doping. Figure 3d shows a series of spectra taken in this manner from 80 nm b-PC nanoribbons. As gate voltage is increased, more carriers are added to the b-PC nanoribbon and the two peaks both increase in intensity and shift to higher frequencies, reaching 1514 and 1710 cm^{-1}, respectively. The carrier density in b-PC nanoribbon was displayed in Figure S2b (see Section 5 in the Supporting Information). Based on the previous work,[7] the plasmon resonance frequency for 2D materials is determined by Fermi level E_F and wavevector q via the equation $\omega_{pl} = \sqrt{e^2 E_F q/(2\pi \hbar^2 \varepsilon_0 \varepsilon_r)}$, where e denotes the elementary unit and ε_0 and ε_r present the dielectric constant for

vacuum and plasmonic material. It demonstrates that when the Fermi level increase, it leads the more carriers to participate into the collective oscillation of plasmons and therefore the blue-shift of both plasmon resonance frequencies. It should be noted that the energy of peak 2 demonstrates a stronger dependence of carrier density as compared to that of peak 1.

For a general understanding of the two observed peaks in experiment, we use a phenomenological model of two coupled classical oscillators to fit the observed transmission spectra, as shown in Figure 4a (see the Supporting Information for details). As a consequence of the coupling effect, the spectrum is not a simple superposition of Lorentzian line shapes from both individual oscillators, but rather a distinctly asymmetric shape with a sharp transparency window in a broad absorption profile, demonstrating a typical character of Fano resonance.[26] Fano resonance is related to the presence of discrete states, that is, IR-active optical phonons in this case, interacting coherently with a broad continuum, that is, plasmon excitation in b-PC nanoribbon. As schematically shown in Figure 4b, the broken inversion symmetry in AB-stacked b-PC nanoribbon leads to a net phonon-induced dipole per unit cell, therefore enabling coherent interactions between collective electrons oscillations (marked by black solid arrows) and lattice vibration modes (marked by black dotted arrows). The best fitted response can be obtained, using a coupling strength of 350 cm^{-1} between the plasmon mode and the phonon mode. To get a quantitative analysis of the proposed physical mechanism, we further studied the HPPP mode in the framework of generalized RPA theory and calculated the loss function $\mathcal{F}[1/\varepsilon_T^{RPA}]$, defined as the imaginary part of the inverse dielectric function, which represents the ability of the system to dissipate energy via
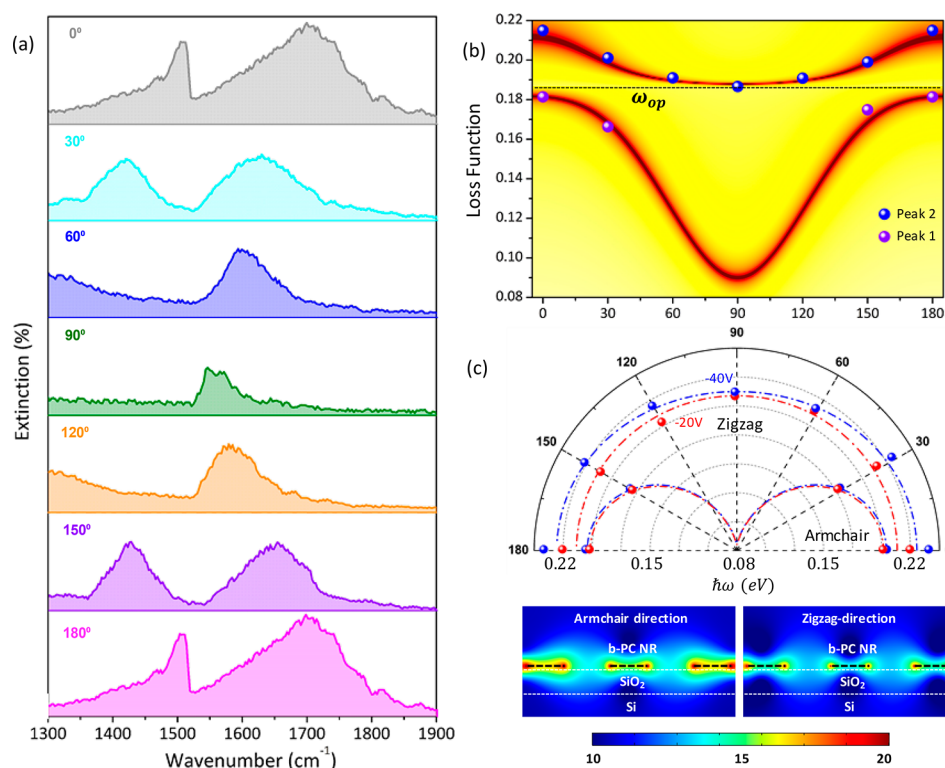
Figure 5. Lattice-orientation-dependence of HPPP behavior in b-PC nanoribbon arrays. (a) Lattice-orientation-dependent modulation of transmission through 80 nm wide b-PC nanoribbon array, with back-gate voltage of −60 V. All of these transmission spectra were normalized to the one obtained at the CNP. (b) Plasmon frequency as a function of lattice orientation for peaks 1 and 2. The experimental results were extracted from (a) (purple and blue square dots for peaks 1 and 2, respectively). The calculated dispersion relation is represented by the loss function and it is plotted as a 2D pseudocolor background. The frequencies of optical mode are marked as horizontal black botted line. (c) Polar intensity plot of plasmon resonance from armchair to zigzag directions and calculated total electric field intensity ($|E|^2$) for b-PC nanoribbon along armchair and zigzag directions using FEM.

plasmon excitations (see the Section 2 in Supporting Information).[1] In a similar fashion of graphene ribbons, we introduce an effective ribbon width defined as $W_e = W − W_0$, where W_0 presents the electrically inactive width caused by the atomic-scale defects or complicated edge chemistry.[27] Figure 4c displays the calculated RPA loss spectra as a function of $q = \pi/W_e$ (assuming $W_0 = 15$ nm) interacting with the phonon resonant frequency ω_{op} and excellent agreement was achieved with experimentally observed plasmon−phonon dispersion collected from Figure 3d. The dashed line represents the plasmon frequency without considering plasmon−phonon hybridization and it can be simply denoted by the scaling law $\omega_{pl} \propto \sqrt{q}$ predicted by the theory.[7] Here, a comparison between the model and experimental data shows clear evidence of splitting of plasmon dispersion due to the hybridization of the plasmon mode with the IR-active optical phonon in b-PC. Similar to HPPP modes in bilayer graphene,[15,27] the intensity of the two peaks changes with the carrier density in b-PC, roughly indicating the characteristics of each hybrid mode, that is, phonon-like mode for peak 1 and plasmon-like mode for peak 2. It describes well the evolution of the plasmon and phonon resonances as they approach each other, evolving from separated resonances to the Fano-like asymmetric spectral line shapes, and eventually an induced splitting of dispersion when their resonant frequencies coincide at ω_{op}.

Since b-PC exhibits anisotropic mobilities along different crystallographic axes, it is naturally anticipated to observe the lattice-orientation-dependent HPPP behavior in b-PC nanoribbon arrays, that is, from armchair to zigzag direction. In

order to eliminate the ribbon configuration induced optical anisotropy, all of these nanoribbons were fabricated with the same width of 80 nm and the incident light polarization was always maintained perpendicularly to b-PC nanoribbons for each angle. To reveal this relationship, we measured the transmission spectra of b-PC nanoribbons oriented from 0° (defined along the armchair direction) to 180° spaced at an angle of 30°, and a prominent periodic variation feature was demonstrated in angle-resolve behavior of HPPP mode, as shown in Figure 5a. Note that the transmission spectra from 60° to 120°, their phonon-like branches cannot be detected as limited to our available measurement scale (limited by minimum wavevector of 1250 cm^{-1}) and their behavior can be validated by following calculation results in Figure 5b. Specifically, when the b-PC nanoribbons vary from 0° to (armchair direction) 90° (zigzag direction), both of the peaks show a redshift of resonance frequency because of an increasing effective mass. Compared with the zigzag direction (green line), the plasmon peak in armchair direction is higher and the resonance line width is narrower. These results suggest that the b-PC is optically more lossy for the zigzag direction, which has been predicted by previous theoretical work.[12] We also calculated the variations of plasmonic performance with different scattering rates and it demonstrates that higher scattering rate leads to the more serious damping to plasmons in b-PC nanoribbons (see Section 6 in Supporting Information). In order to understand the anisotropic behavior of plasmon resonance in b-PC nanoribbons, Figure 5b shows the angular dependence of wavevector q on the HPPP behavior

by plotting the loss function, for $W = 80$ nm. The results show that the maximum value of loss function occurs at around $\theta = 0°$ and $180°$. Furthermore, we calculated the electromagnetic profile using FEM along the armchair and zigzag directions, respectively. Figure 5c plots the amplitude of the $|E|^2$ for linear polarization which clearly illustrates the electric dipole behavior confined around the edges of b-PC ribbon, indicating a plasmon resonance behavior. It can be seen that the localized electrical field around the two edges of armchair-oriented b-PC nanoribbons is much stronger that the one along zigzag direction, which is consistent with our experimental results.

In summary, we have introduced a new class of anisotropic 2D material, b-PC, to serve as a promising candidate capable of supporting tunable anisotropic plasmons. The few-layer b-PC in the nanoribbon configuration was studied and two electrically tunable resonances were resolved in the IR transmission spectroscopy, which were caused by a Fano resonance-induced HPPP mode. Numerical calculations confirm the experimental observations and further reveal the origin of HPPP mode from the coupling between collective electrons oscillation and the IR-active optical phonon mode in AB-stacked b-PC nanoribbons. The presented experimental and simulation results further illustrate the lattice-orientation-dependence of HPPP, demonstrating a prominent redshift of plasmon frequency from armchair to zigzag direction. Our work demonstrates that the intrinsic in-plane anisotropy of b-PC can provide a natural platform to engineer the plasmonic performance, leading to a new degree of freedom for which the light−matter interactions can be manipulated in dynamically reconfigurable directions to offer new functionalities in novel optical and optoelectronic device applications beyond conventional materials and approaches.[28]

ASSOCIATED CONTENT

Ⓢ Supporting Information

The Supporting Information is available free of charge on the ACS Publications website at DOI: 10.1021/acsphotonics.8b00353.

> Details of first-principles computation for phonon mode in AB-stacked b-PC; Device fabrication of black phosphorus carbide (b-PC) nanoribbon arrays; Model of coupled oscillator model for the plasmon−phonon coupling system; Calculation details of the RPA dielectric function and loss function; Calculation of carbon concentration and carrier density in b-PC nanoribbon; Analysis of relation between mobility and plasmonic performance in b-PC nanoribbon (PDF).

AUTHOR INFORMATION

Corresponding Author
*E-mail: eleakw@nus.edu.sg.

ORCID Ⓘ
Xin Huang: 0000-0003-2065-6384
Lin Wang: 0000-0003-3430-7345
Li Huang: 0000-0002-2188-3178
Christian A. Nijhuis: 0000-0003-3435-4600
Chengkuo Lee: 0000-0002-8886-3649
Kah-Wee Ang: 0000-0003-1919-3351

Author Contributions
K.W.A. supervised the project. X.H. conceived and designed the project. X.F., W.C.T., L.C., L.W., and L.H. assisted to prepare the samples and device fabrication. D.N.H., N.C., and C.L. assisted to perform FTIR measurements. Y.C. and Y.W.Z. performed the DFT calculations and analysis of phonon modes in b-PC. D.N.H., N.C., T.J.D., and C.A.N. discussed the physical mechanism of plasmon−phonon coupling in b-PC. All authors contributed to the scientific discussions and manuscript reparation.

Notes
The authors declare no competing financial interest.

REFERENCES

(1) Low, T.; Chaves, A.; Caldwell, J. D.; Kumar, A.; Fang, N. X.; Avouris, P.; Heinz, T. F.; Guinea, F.; Martin-Moreno, L.; Koppens, F. Polaritons in layered two-dimensional materials. *Nat. Mater.* **2017**, *16*, 182−194.

(2) Ju, L.; Geng, B.; Horng, J.; Girit, C.; Martin, M.; Hao, Z.; Bechtel, H. A.; Liang, X.; Zettl, A.; Shen, Y. R.; Wang, F. Graphene plasmonics for tunable terahertz metamaterials. *Nat. Nanotechnol.* **2011**, *6*, 630−634.

(3) Nikitin, A. Y.; Guinea, F.; García-Vidal, F.; Martín-Moreno, L. Edge and waveguide terahertz surface plasmon modes in graphene microribbons. *Phys. Rev. B: Condens. Matter Mater. Phys.* **2011**, *84*, 161407.

(4) Freitag, M.; Low, T.; Zhu, W.; Yan, H.; Xia, F.; Avouris, P. Photocurrent in graphene harnessed by tunable intrinsic plasmons. *Nat. Commun.* **2013**, *4*, 1951.

(5) Rodrigo, D.; Limaj, O.; Janner, D.; Etezadi, D.; de Abajo, F. J. G.; Pruneri, V.; Altug, H. Mid-Infrared Plasmonic Biosensing with Graphene. *Science* **2015**, *349*, 165−168.

(6) Hu, H.; Yang, X.; Zhai, F.; Hu, D.; Liu, R.; Liu, K.; Sun, Z.; Dai, Q. Far-field nanoscale infrared spectroscopy of vibrational fingerprints of molecules with graphene plasmons. *Nat. Commun.* **2016**, *7*, 12334.

(7) Low, T.; Roldán, R.; Wang, H.; Xia, F.; Avouris, P.; Moreno, L. M.; Guinea, F. Plasmons and screening in monolayer and multilayer black phosphorus. *Phys. Rev. Lett.* **2014**, *113*, 106802.

(8) Saberi-Pouya, S.; Vazifehshenas, T.; Salavati-Fard, T.; Farmanbar, M.; Peeters, F. M. Strong anisotropic optical conductivity in two-dimensional puckered structures: The role of the Rashba effect. *Phys. Rev. B: Condens. Matter Mater. Phys.* **2017**, *96*, 075411.

(9) Saberi-Pouya, S.; Vazifehshenas, T.; Salavati-fard, T.; Farmanbar, M. Anisotropic hybrid excitation modes in monolayer and double-layer phosphorene on polar substrates. *Phys. Rev. B: Condens. Matter Mater. Phys.* **2017**, *96*, 115402.

(10) Abate, Y.; Gamage, S.; Li, Z.; Babicheva, V.; Javani, M. H.; Wang, H.; Cronin, S. B.; Stockman, M. I. Nanoscopy reveals surface-metallic black phosphorus. *Light: Sci. Appl.* **2016**, *5*, e16162.

(11) Huber, M. A.; Mooshammer, F.; Plankl, M.; Viti, L.; Sandner, F.; Kastner, L. Z.; Frank, T.; Fabian, J.; Vitiello, M. S.; Cocker, T. L.; Huber, R. Femtosecond photo-switching of interface polaritons in black phosphorus heterostructures. *Nat. Nanotechnol.* **2017**, *12*, 207−211.

(12) Wang, G.; Pandey, R.; Karna, S. P. Carbon phosphide monolayers with superior carrier mobility. *Nanoscale* **2016**, *8*, 8819−8825.

(13) Tan, W. C.; Cai, Y.; Ng, R. J.; Huang, L.; Feng, X.; Zhang, G.; Zhang, Y. W.; Nijhuis, C. A.; Liu, X.; Ang, K. W. Few-Layer Black Phosphorus Carbide Field-Effect Transistor via Carbon Doping. *Adv. Mater.* **2017**, *29*, 1700503.

(14) Dai, S.; Ma, Q.; Liu, M. K.; Andersen, T.; Fei, Z.; Goldflam, M. D.; Wagner, M.; Watanabe, K.; Taniguchi, T.; Thiemens, M.; Keilmann, F. Graphene on hexagonal boron nitride as a tunable hyperbolic metamaterial. *Nat. Nanotechnol.* **2015**, *10*, 682−686.

(15) Bezares, F. J.; Sanctis, A. D.; Saavedra, J. R.; Woessner, A.; Alonso-González, P.; Amenabar, I.; Chen, J.; Bointon, T. H.; Dai, S.; Fogler, M. M.; Basov, D. N. Intrinsic Plasmon-Phonon Interactions in Highly Doped Graphene: A Near-Field Imaging Study. *Nano Lett.* **2017**, *17*, 5908−5913.

(16) Ozbay, E. Plasmonics: merging photonics and electronics at nanoscale dimensions. *Science* **2006**, *311*, 189−193.

(17) Forati, E.; Hanson, G. W.; Yakovlev, A. B.; Alu, A. Planar hyperlens based on a modulated graphene monolayer. *Phys. Rev. B: Condens. Matter Mater. Phys.* **2014**, *89*, 081410.

(18) Xia, F.; Wang, H.; Xiao, D.; Dubey, M.; Ramasubramaniam, A. Two-dimensional material nanophotonics. *Nat. Photonics* **2014**, *8*, 899−907.

(19) Tan, W. C.; Huang, L.; Ng, R. J.; Wang, L.; Hasan, D. M.; Duffin, T. J.; Kumar, K. S.; Nijhuis, C. A.; Lee, C.; Ang, K. W. A Black Phosphorus Carbide Infrared Phototransistor. *Adv. Mater.* **2018**, *30*, 1705039.

(20) Claeyssens, F.; Fuge, G. M.; Allan, N. L.; May, P. W.; Ashfold, M. N. R. Phosphorus carbides: theory and experiment. *Dalton Trans.* **2004**, *19*, 3085−3092.

(21) Guan, J.; Liu, D.; Zhu, Z.; Tomanek, D. Two-Dimensional Phosphorus Carbide: Competition between sp^2 and sp^3 Bonding. *Nano Lett.* **2016**, *16*, 3247−3252.

(22) Nikitin, A. Y.; Guinea, F.; Garcia-Vidal, F. J.; Martin-Moreno, L. Surface plasmon enhanced absorption and suppressed transmission in periodic arrays of graphene ribbons. *Phys. Rev. B: Condens. Matter Mater. Phys.* **2012**, *85*, 081405.

(23) Wang, V.; Kawazoe, Y.; Geng, W. T. Native point defects in few-layer phosphorene. *Phys. Rev. B: Condens. Matter Mater. Phys.* **2015**, *91*, 045433.

(24) Brar, V. W.; Jang, M. S.; Sherrott, M.; Kim, S.; Lopez, J. J.; Kim, L. B.; Choi, M.; Atwater, H. Hybrid surface-phonon-plasmon polariton modes in graphene/monolayer h-BN heterostructures. *Nano Lett.* **2014**, *14*, 3876−3880.

(25) Fei, Z.; Goldflam, M. D.; Wu, J. S.; Dai, S.; Wagner, M.; McLeod, A. S.; Liu, M. K.; Post, K. W.; Zhu, S.; Janssen, G. C. A. M.; Fogler, M. M. Edge and Surface Plasmons in Graphene Nanoribbons. *Nano Lett.* **2015**, *15*, 8271−8276.

(26) Luk'yanchuk, B.; Zheludev, N. I.; Maier, S. A.; Halas, N. J.; Nordlander, P.; Giessen, H.; Chong, C. T. The Fano resonance in plasmonic nanostructures and metamaterials. *Nat. Mater.* **2010**, *9*, 707−715.

(27) Yan, H.; Low, T.; Guinea, F.; Xia, F.; Avouris, P. Tunable phonon-induced transparency in bilayer graphene nanoribbons. *Nano Lett.* **2014**, *14*, 4581−4586.

(28) Sun, Z.; Martinez, A.; Wang, F. Optical modulators with 2D layered materials. *Nat. Photonics* **2016**, *10*, 227−238.